ANNUAL REVIEWS

Annual Review of Nuclear and Particle Science

Nuclear Dynamics and Reactions in the Ab Initio Symmetry-Adapted Framework

Kristina D. Launey,[1] Alexis Mercenne,[1,2] and Tomas Dytrych[1,3]

[1]Department of Physics and Astronomy, Louisiana State University, Baton Rouge, Louisiana 70803, USA; email: klauney@lsu.edu

[2]Center for Theoretical Physics, Sloane Physics Laboratory, Yale University, New Haven, Connecticut 06520, USA

[3]Nuclear Physics Institute of the Czech Academy of Sciences, 250 68 Řež, Czech Republic

Annu. Rev. Nucl. Part. Sci. 2021. 71:253–77

First published as a Review in Advance on June 29, 2021

The *Annual Review of Nuclear and Particle Science* is online at nucl.annualreviews.org

https://doi.org/10.1146/annurev-nucl-102419-033316

Keywords

ab initio symmetry-adapted framework, nuclear structure and reactions, nuclear shapes and deformation, decay widths and α-capture reactions, X-ray burst abundances, nucleon–nucleus potentials

Abstract

We review the ab initio symmetry-adapted (SA) framework for determining the structure of stable and unstable nuclei, along with related electroweak, decay, and reaction processes. This framework utilizes the dominant symmetry of nuclear dynamics, the shape-related symplectic Sp(3, $\mathbb{R}$) symmetry, which has been shown to emerge from first principles and to expose dominant degrees of freedom that are collective in nature, even in the lightest species or seemingly spherical states. This feature is illustrated for a broad scope of nuclei ranging from helium to titanium isotopes, enabled by recent developments of the ab initio SA no-core shell model expanded to the continuum through the use of the SA basis and that of the resonating group method. The review focuses on energies, electromagnetic transitions, quadrupole and magnetic moments, radii, form factors, and response function moments for ground-state rotational bands and giant resonances. The method also determines the structure of reaction fragments that is used to calculate decay widths and α-capture reactions for simulated X-ray burst abundance patterns, as well as nucleon–nucleus interactions for cross sections and other reaction observables.

Contents

1. INTRODUCTION

A fundamental new feature of atomic nuclei has recently been established and shown to emerge naturally from first principles (1). Specifically, ab initio large-scale calculations have revealed a remarkably ubiquitous and only slightly broken symmetry, the Sp(3, $\mathbb{R}$) symplectic symmetry, in nuclei up through the calcium region [anticipated to hold even more strongly in heavy nuclei (2)]. Since this symmetry does not mix nuclear shapes, the novel nuclear feature provides important insight from first principles into the physics of nuclei and their low-lying excitations as dominated by only a few collective shapes—equilibrium shapes with their vibrations—that rotate (**Figure 1*a***).

This remarkable outcome builds upon decades-long research, starting with pivotal work by Draayer and colleagues (3–6) and Rowe and Rosensteel (2, 7–9), who successfully harnessed group theory as a powerful tool for understanding and computing the intricate structure of nuclei. This pioneering research has been instrumental in designing the theory that underpins many highly ordered patterns revealed through a large body of experimental data (10–12), while explaining phenomena observed in energy spectra, *E*2 transitions and deformation, giant resonances (GR), scissor modes and *M*1 transitions, electron scattering form factors, and the interplay of pairing with collectivity. These new developments and insights built the critical structure raised upon the foundation laid by Elliott (13–15) and Hecht and colleagues (16, 17) and paved the way toward large-scale calculations feasible today on supercomputers. Now, within an ab initio framework without a priori symmetry assumptions, the symmetry-adapted no-core shell model (SA-NCSM) (6, 18, 19) with chiral effective field theory (EFT) interactions (20–22) not only explains but also predicts the emergence of nuclear collectivity across nuclei, even in close-to-spherical nuclear states without any recognizable rotational properties.

The symmetry-adapted (SA) framework (1, 6, 18), discussed in Section 3, capitalizes on these findings and presents solutions in terms of a physically relevant basis of nuclear shapes. By exploiting this approximate symmetry, the SA framework resolves the scale explosion problem in nuclear structure calculations, that is, the explosive growth in computational resource demands with an increase in both the number of particles and the size of the spaces in which they reside (referred to as model spaces). It is based on the idea that the infinite Hilbert space can be equivalently spanned by microscopic nuclear shapes and their rotations [or symplectic

GR: giant resonance(s)

SA-NCSM: symmetry-adapted no-core shell model

EFT: effective field theory

SA: symmetry-adapted

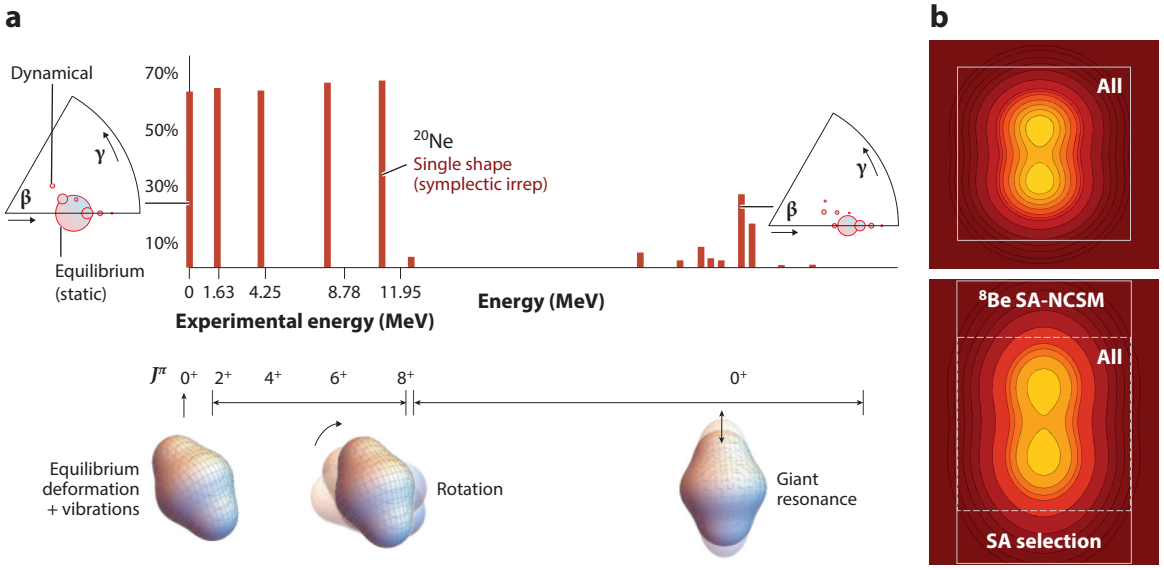

Figure 1

(*a*) Contribution of the most dominant shape to the 0^+ ground state of ^{20}Ne and its rotational band (2^+, 4^+, 6^+, and 8^+), as well as to excited 0^+ states, pointing to a fragmented giant monopole resonance. For selected states, the deformation distribution within a shape is shown in terms of the shape parameters, the average deformation β and triaxiality angle γ (based on ab initio SA-NCSM calculations with NNLO_{opt} in a model space of 11 harmonic oscillator shells with an intershell distance of $\hbar\Omega = 15$ MeV). (*b*) Schematic illustration of the SA concept for ^{8}Be. (*Top*, *square*) A smaller model space includes all possible shapes (labeled "All") and yields spatially compressed wave functions. (*Bottom*, *rectangle*) A larger model space accommodates, in a well-prescribed way, spatially extended modes (labeled "SA selection") that are neglected in smaller model spaces. Abbreviations: irrep, irreducible representation; SA, symmetry-adapted; SA-NCSM, symmetry-adapted no-core shell model. Panel *a* adapted with permission from Reference 1.

irreducible representations (irreps), subspaces that preserve the symmetry]; here, the term microscopic refers to the fact that these configurations track with position and momentum coordinates of each particle. A collective nuclear shape can be viewed as an equilibrium (static) deformation and its vibrations (dynamical deformations) of the GR type (see Section 3.1), as illustrated in the β–γ plots in **Figure 1*a*** (1, 23). **Figure 1*b*** illustrates a key component of the SA concept: While many shapes relevant to low-lying states are included in typical shell-model spaces, the vibrations of largely deformed equilibrium shapes and spatially extended modes like clustering often lie outside such spaces. The selected model space in the SA framework remedies this problem and includes those configurations in a well-prescribed way. Note that this is critical for enhanced deformation, since spherical and less deformed shapes easily develop in comparatively small model-space sizes.

Ab initio descriptions of spherical and deformed nuclei up through the calcium region are now possible without the use of interaction renormalization procedures, as discussed in Section 3. In particular, References 6, 19, and 24–26 have shown that the SA-NCSM can use model spaces significantly smaller than the corresponding ultralarge conventional model spaces without compromising the accuracy of results for various observables, allowing the SA-NCSM to accommodate larger model spaces and to reach heavier nuclei, such as ^{20}Ne (1), ^{21}Mg (27), ^{22}Mg (28), and ^{28}Mg (29), as well as ^{32}Ne and ^{48}Ti (30).

For this reason, the SA basis is especially suitable for describing nuclear reactions, which is key to understanding processes measured in experiments and those in extreme environments ranging

irrep: irreducible representation

Collective nuclear shape: equilibrium shape and its vibrations, which, together with its rotations, span a single $\text{Sp}(3,\mathbb{R})$ irrep

Static deformation: equilibrium shape, invariant under $\text{Sp}(3,\mathbb{R})$ transformations

Dynamical deformation: GR-type vibration of an equilibrium shape

XRB: X-ray burst

SA-RGM: symmetry-adapted resonating group method

RGM: resonating group method

from stellar explosions to the interior of nuclear reactors. Recently, remarkable progress has been made in first-principles many-body approaches to scattering and nuclear reactions for light nuclei (for an overview, see 31), including studies of elastic scattering (32–36), photoabsorption (37), transfer (38) and capture (39) reactions, and thermonuclear fusion (40). Expanding the reach of ab initio reactions beyond the lightest species, including deformed targets (from helium to calcium isotopes) and α projectiles, is now feasible with the SA basis, and we review three recent developments in Section 4. We start with a remarkable illustration, namely the first description of the α+^{16}O system based on ab initio SA-NCSM descriptions of ^{20}Ne, along with an estimate of the α-capture reaction rate ^{16}O(α,γ)^{20}Ne at temperatures relevant to X-ray burst (XRB) nucleosynthesis (41).

For a single-nucleon projectile, the SA basis plays a key role in the recently developed ab initio symmetry-adapted resonating group method (SA-RGM) (42, 43) for cross sections of reactions and scattering at low energy, which is the astrophysically relevant energy regime. The SA-RGM follows the successful merging of the resonating group method (RGM) (44) with the no-core shell model (NCSM) for light nuclei (45), which provided unified descriptions of structure and reaction observables from first principles. The SA-RGM utilizes the same symmetry considerations as for the SA-NCSM and, in doing so, affords this approach the capability to simultaneously describe both bound and scattering states, while preserving the Pauli exclusion principle and translational invariance (see Section 4.2.1 for the n+^{16}O and n+^{20}Ne systems, with a focus on low-lying resonant and scattering states). For the intermediate-energy regime, which corresponds to current experimental studies at rare isotope beam facilities, the spectator expansion of the multiple scattering theory (46, 47) has recently offered a fully consistent ab initio approach to nucleon scattering that accounts for both the spin of the struck nucleon in the target (48) and the microscopic structure of the target from first principles by utilizing ab initio one-body nuclear densities (49; see Section 4.2.2 for proton scattering on ^{4}He and ^{20}Ne targets, at projectile laboratory energies of 100–200 MeV per nucleon). As an important outcome, these frameworks offer a way to construct nucleon–nucleus effective interactions rooted in first principles, the key component of reaction theory (see Section 2).

The overarching goal is, by exploiting dominant symmetries in nuclear dynamics and the SA basis, to provide reliable descriptions of nuclear reactions that can be measured at rare isotope beam facilities and are of particular interest in astrophysics. For example, the proton-capture ^{23}Al(p,γ)^{24}Si reaction is one of several reactions determined to have a substantial effect on luminosity profiles in time (light curves) from XRB nucleosynthesis simulations (50, 51). Predictions for XRB light curves are important because they are available from observational astronomy (e.g., 52). Equally important are (α,p), (α,n), and (α,γ) reactions (53, 54), such as the ^{12}C(α,γ)^{16}O reaction rate (55). The latter is one of the most important reactions for stellar helium burning, and it currently has uncertainties that could affect the predicted accuracy of the final black hole mass (56, 57) in analyses of current and upcoming gravitational-wave interferometer detections of binary black hole mergers (58). Furthermore, measuring neutron-capture cross sections is critical for astrophysical simulations that aim to resolve the r-process (59). While direct capture measurements with exotic isotopes are often not possible because of practical considerations, such as very small cross sections, the unavailability of beams, or the infeasibility of measuring neutron-induced reactions on radioactive isotopes, the one-nucleon transfer reaction (d, p) has been proposed as a suitable indirect tool for providing information about cross sections for neutron-capture reactions (e.g., 60, 61). In addition, the use of n+^{48}Ca scattering and total neutron cross-section measurements can place constraints on the neutron skin thickness (62), important for pinpointing the equation of state of neutron-star matter (e.g., 63).

RARE ISOTOPE BEAM FACILITIES AND THE NEED FOR THEORY

Experiments at existing and future rare isotope beam facilities can probe nucleon–nucleon interactions and nuclear structure, but they require novel theoretical approaches that can reliably model reactions of short-lived isotopes to support and inform experimental programs. Historically, two cornerstone frameworks have been employed. First, few-body techniques (with early applications to reactions) use correct asymptotics (i.e., the wave function of the reaction fragments at long distances), but may often neglect the microscopic structure of the clusters and employ optical potentials fitted to elastic scattering data of stable nuclei (e.g., 64–66). Second, many-body techniques (with early applications to structure) use many-body degrees of freedom and target unified structure and reaction descriptions, but may often neglect or only partially account for the continuum, and are often limited in mass or number of active particles as a result of increased complexity. Recent developments have begun to address many of these challenges by merging these concepts, through the inclusion of microscopic degrees of freedom in few-body models, construction of microscopic few-body effective interactions (optical potentials) (48, 67, 68), and incorporation of continuum and collective degrees of freedom into many-body approaches (40–42, 69, 70). Several recent experimental and theoretical white papers summarize the new physics to be learned from proposed experiments and new theoretical developments for unstable nuclei (see 31, 71, 72, and references therein).

2. NUCLEAR APPROACHES IN THE ERA OF RARE ISOTOPE BEAM FACILITIES

Currently, only a small fraction of the thousands of nuclei that exist can be measured and described reasonably well by theory. Most of these lie in the so-called valley of stability. This underscores the need for exploration of and beyond the drip lines, that is, the limit of nuclear stability with respect to the emission of one nucleon. Measuring and describing nuclei far from stability are indeed very important for nuclear astrophysics, as many short-lived nuclei are formed during cataclysmic events in the Universe and can, in turn, significantly influence various astrophysics simulations. Because measurements involve scattering and reactions of nuclei, it is important to have a reliable and predictive theoretical framework of reaction processes that is applicable to both stable and unstable nuclei (see the sidebar titled Rare Isotope Beam Facilities and the Need for Theory).

Exact solutions for the scattering problem are available only for systems with up to five nucleons (73–76). Nuclear approaches to reactions and scattering face several challenges, especially since nuclear probes are often peripheral and hence require a correct asymptotic treatment. Major challenges include the long-range Coulomb force, especially in the case of large projectile and/or target charges where the asymptotics may not be analytically known; the high sensitivity of reaction observables to reaction thresholds (Q values); the importance of the nonresonant continuum when nuclei break up into the continuum; and difficulties in describing scattering state asymptotics with single-particle bound-state bases typically used in many-body methods (31).

Currently, many successful reaction models employ approximations and rely largely on constraints from data (phenomenology), including R-matrix methods, Glauber theory, the Hauser–Feshbach model, phenomenological optical models, and the valence shell model. While these methods have been very successful in certain mass regions and energies across the valley of stability, they are often limited by the approximations they assume. For example, the Hauser–Feshbach model assumes high level densities; phenomenological optical potentials do well at comparatively high projectile energies, whereas at low energies they fail to account appropriately for isolated resonances [in addition, they are fitted to stable nuclei, and uncertainties become uncontrolled as one moves away from stability (77)]; reaction models often assume no structure of the clusters;

and valence shell-model calculations omit particle–hole excitations that are expected to play an important role in weakly bound systems.

Alternatively, one can employ many-nucleon approaches with controlled approximations (for recent reviews, see, e.g., 31, 78). These include the use of a physically relevant basis, such as the SA basis, that accommodates model spaces large enough to describe the wave-function tail within the potential effective range [while at long distances the exact Coulomb wave functions are used (41; see Section 4.1)]; adding a basis that explicitly considers the reaction fragments, such as the RGM basis (34, 40, 42, 45; see Section 4.2.1); and starting with a complex-momentum single-particle basis, such as the Berggren basis (e.g., 69, 70, 79–81), which imposes single-particle scattering boundary conditions, thereby consistently treating bound states, resonances, and scattering states within the same framework. However, these methods are often limited by computational resources and may not achieve the required level of accuracy. In such cases, it might be advantageous to adopt a hybrid approach that allows some quantities to be directly taken from (or strongly constrained by) data, such as threshold measurements. Thus, for example, experiments can provide precise thresholds, whereas theory can pinpoint critical collective and clustering correlations in wave functions to achieve the best estimates of reaction rates for astrophysics. Indeed, to analyze and interpret experimental data, theory with uncertainties lower than 10% is needed (31).

3. SYMMETRY-ADAPTED FRAMEWORK AND ROLE OF SYMPLECTIC SYMMETRY

3.1. Symmetry-Adapted No-Core Shell Model

Ab initio approaches build upon a first-principles foundation, specifically, the properties of only two or three nucleons that are often tied to symmetries and symmetry-breaking patterns of the underlying quantum chromodynamics theory. We utilize the ab initio nuclear shell-model theory (82, 83) that solves the many-body Schrödinger equation for A particles:

$$H\Psi(\vec{r}_1,\vec{r}_2,\ldots,\vec{r}_A) = E\Psi(\vec{r}_1,\vec{r}_2,\ldots,\vec{r}_A), \text{with } H = T_{\rm rel} + V_{NN} + V_{3N} + \cdots + V_{\rm Coulomb}. \quad 1.$$

In its most general form, this is an exact many-body configuration interaction method, for which the interaction and basis configurations are as follows. The intrinsic nonrelativistic nuclear Hamiltonian H includes the relative kinetic energy $T_{\rm rel} = (1/A)\sum_{i<j}^{A}(\vec{p}_i - \vec{p}_j)^2/2m$ (where m is the nucleon mass); the nucleon–nucleon (NN) and possibly three-nucleon ($3N$) interactions, typically

DEFORMATION-RELATED SU(3) AND SHAPE-RELATED SYMPLECTIC Sp(3, $\mathbb{R}$) GROUPS

A collective nuclear shape is microscopically described by a set of A-particle configurations that preserves the Sp(3, $\mathbb{R}$) symmetry and includes an equilibrium deformation and its vibrations, the dynamical deformations, along with rotations (1, 23). From a mathematical point of view, the symplectic group Sp(3, $\mathbb{R}$) consists of all particle-independent linear canonical transformations of the single-particle phase-space observables, the positions $\vec{r}_i$ and momenta $\vec{p}_i$, that preserve the Heisenberg commutation relations $[r_{i\alpha}, p_{j\beta}] = i\hbar\delta_{ij}\delta_{\alpha\beta}$ (with particle index $i = 1,\ldots,A$ and spatial directions $\alpha, \beta = x, y, z$) (2, 6, 23). A key feature is that several physically relevant operators do not mix nuclear shapes, including the total kinetic energy, $p^2/2 = (1/2)\sum_{i=1}^{A}(p_i^2)$; the monopole moment, $r^2 = \sum_{i=1}^{A}(r_i^2)$; the quadrupole moment, $Q_{2M} = \sqrt{16\pi/5}\sum_{i=1}^{A} r_i^2 Y_{2M}(\hat{r}_i)$; the orbital momentum, $\vec{L} = \sum_{i=1}^{A}\vec{r}_i \times \vec{p}_i$; and the many-body HO Hamiltonian, $H_0 = (p^2/2) + (r^2/2)$. A subset of these act only within a single deformation or an SU(3) irrep, specifically the operators Q_{2M} (when restricted to a single shell) and L.

derived in the chiral EFT (20–22); and the Coulomb interaction between the protons. A complete orthonormal many-particle basis ψ_k is adopted, for instance, the antisymmetrized products of single-particle states of a spherical harmonic oscillator (HO) of characteristic length $b = \sqrt{\hbar/m\Omega}$ and frequency Ω. The expansion $\Psi(\vec{r}_1, \vec{r}_2, \ldots, \vec{r}_A) = \sum_k c_k \psi_k(\vec{r}_1, \vec{r}_2, \ldots, \vec{r}_A)$ transforms Equation 1 to a matrix eigenvalue equation, $\sum_{k'} H_{kk'} c_{k'} = E c_k$, with unknowns c_k, where the many-particle Hamiltonian matrix elements $H_{kk'} = \langle \psi_k | H | \psi_{k'} \rangle$ are calculated for the given interaction and the solution $\{c_k^2\}$ defines a set of probability amplitudes.

NN: nucleon–nucleon

3N: three-nucleon

HO: harmonic oscillator

Throughout this review, we adopt the term ab initio for a system of A particles in cases when an A-body approach with controlled approximations is employed, such as the SA-NCSM, together with realistic interactions that reproduce NN phase-shift data to a given energy with high precision (and perhaps properties of $3N$ systems). These include JISP16 (84) and AV18 (85), as well as the chiral potentials N3LO-EM (22), NNLO_{opt} (86), and NNLO_{sat} (87), including the complementary $3N$ forces.

An important feature of the SA framework is that the model space is reorganized into an SA basis that respects the deformation-related SU(3) symmetry or the shape-related $\text{Sp}(3,\mathbb{R})$ symmetry [6; see the sidebar titled Deformation-Related SU(3) and Shape-Related Symplectic $\text{Sp}(3,\mathbb{R})$ Groups]. Note that while the model utilizes symmetry groups to construct the basis, calculations are not limited a priori by any symmetry and employ a large set of basis states that can, if the nuclear Hamiltonian demands it, describe a significant symmetry breaking. The SA-NCSM (reviewed in 6) was first applied to light nuclei using the SU(3)-adapted basis (19) and soon thereafter was expanded with an $\text{Sp}(3,\mathbb{R})$-adapted basis and to heavier nuclei (1, 6). Both bases are briefly discussed next.

3.1.1. SU(3)-adapted basis. The many-nucleon basis states of the SA-NCSM are constructed using efficient group-theoretical algorithms and are labeled according to $\text{SU}(3)_{(\lambda\,\mu)} \times \text{SU}(2)_S$ by the total intrinsic spin S and $(\lambda\,\mu)$ quantum numbers with $\lambda = N_z - N_x$ and $\mu = N_x - N_y$, where $N_x + N_y + N_z = N_0 + N$, for a total of $N_0 + N$ HO quanta distributed in the x, y, and z directions. Here, $N_0\hbar\Omega$ is the lowest total HO energy for all particles (valence-shell configuration), and $N\hbar\Omega$ ($N \leq N_{\max}$) is the additional HO energy of all particle–hole excitations. Thus, $N_x = N_y = N_z$, or equivalently $(\lambda\,\mu) = (0\,0)$, describes a spherical configuration, while a value of N_z larger than $N_x = N_y$ ($\mu = 0$) indicates prolate deformation. Clearly, a closed-shell configuration has $(0\,0)$, and spherical shapes (or no deformation) are a part of the SA basis. However, most nuclei—from light to heavy—are deformed in the *body-fixed* frame ($N_z > N_x > N_y$), which for 0^+ states appears spherical in the laboratory frame.

3.1.2. $\text{Sp}(3,\mathbb{R})$-adapted basis. Considering the embedding $\text{Sp}(3,\mathbb{R})$ symmetry according to $\text{Sp}(3,\mathbb{R}) \supset \text{SU}(3)$, one can further organize SU(3) deformed configurations into symplectic irreps, subspaces that preserve the $\text{Sp}(3,\mathbb{R})$ symmetry. A symplectic irrep is characterized by a given equilibrium shape, labeled by a single deformation $N(\lambda\,\mu)$. For example, a symplectic irrep $0(8\,0)$ in ^{20}Ne consists of a prolate $0(8\,0)$ equilibrium shape with $\lambda = 8$ and $\mu = 0$ in the valence-shell zero-particle zero-hole (0p–0h) subspace, along with many other SU(3) deformed configurations (vibrations), such as $2(10\,0)$, $2(6\,2)$, and $8(16\,0)$, that include particle–hole excitations of the equilibrium shape to higher shells (for further details, see 1, 6, 88). These vibrations are multiples of $2\hbar\Omega$ 1p–1h excitations of the GR monopole and quadrupole types; that is, they are induced by the monopole r^2 and quadrupole Q operators, respectively.

A major advantage of the SA-NCSM is that the SA model space can be downselected to a subset of SA basis states that describe equilibrium and dynamical deformation, and within this selected model space the spurious center-of-mass motion can be factored out exactly (89, 90). Another major advantage is that deformation and collectivity are properly treated in this approach

without the need to break and restore rotational symmetry. The reason is that basis states utilize the SU(3) ⊃ SO(3) reduction chain, which has a good orbital momentum, whereas all SU(3) reduced matrix elements depend only on $(\lambda\,\mu)$ and can be calculated in the simpler canonical SU(3) ⊃ SU(2) reduction chain, which takes advantage of the Cartesian scheme (N_z, N_x, N_y). A third major advantage is the use of group theory, including the Wigner–Eckart theorem and group-theoretical algorithms (e.g., 91–93).

3.2. Unveiling Dominant Features and Symmetries: Equilibrium Shapes, Vibrations, and Rotations

As mentioned above, recent first-principles SA-NCSM calculations below the calcium region revealed the remarkable result that nuclei exhibit relatively simple physics (1). We now understand that a low-lying nuclear state is composed predominantly of a few equilibrium shapes that vibrate through excitations of the GR monopole and quadrupole types, and also rotate (see also 94, 95). Specifically, nuclei are predominantly—typically in excess of 70–80%—composed of only a few shapes. They are often composed of a single shape (a single symplectic irrep), as in the odd–odd nuclei ^{6}Li (**Figure 2*a***) and ^{8}B, the cluster-like ^{8}Be (**Figure 1*b***), ^{16}O (often considered to be closed-shell), and the intermediate-mass ^{20}Ne (**Figures 1*a*, 2*b***). Two shapes are found, for instance, in ^{8}He (generally considered to be spherical) and ^{12}C [24; see also results in 6 and 95 based on SU(3) analysis]. Furthermore, the ground state of ^{6}Li and ^{20}Ne (^{16}O) has a dominant prolate (spherical) shape, while an oblate shape dominates in the cases of ^{8}He and ^{12}C. The symplectic symmetry holds even in excited states (88) and for ^{7}Be (96).

In addition to the predominant irrep(s), there is a manageable number of symplectic irreps, each of which contributes at a level that is typically at least an order of magnitude smaller, as discussed in Reference 1. In addition, this study (1) has shown that realistic interactions yield practically the same symplectic content in low-lying states as the one observed in the ground state (see **Figure 1*a*** for 2^+, 4^+, 6^+, and 8^+), which is a rigorous signature of rotations of a shape and can be used to identify members of a rotational band.

Exploiting the approximate symplectic symmetry allows excitation energies and $B(E2)$ transition strengths to be studied for selected nuclei with the use of only a few symplectic irreps or SU(3) model spaces (which include all symplectic irreps), as shown in **Figure 2** for ^{6}Li and ^{20}Ne. Within a few symplectic irreps, these observables show a relatively fast convergence trend across variations in model-space size and resolution (related to $N_{\max}$ and $\hbar\Omega$) (1, 88), yielding extrapolations to infinitely many shells with typical errors of ∼100 keV for excitation energies and ∼4% for $B(E2)$. Note that $E2$ transitions are determined by the quadrupole operator Q, an $\mathrm{Sp}(3,\mathbb{R})$ generator that does not mix symplectic irreps—the predominance of a single symplectic irrep leads to the remarkable result that the largest fraction of these transitions, and hence nuclear collectivity, necessarily emerges within this symplectic irrep [similarly for root-mean-square (rms) radii, since r^2 is also an $\mathrm{Sp}(3,\mathbb{R})$ generator].

Note the small model-space size used for computations of low-lying states in ^{6}Li and ^{20}Ne (**Figure 2**). For comparison, the corresponding NCSM dimension for $J^\pi = 0^+$, 2^+, and 4^+ in ^{20}Ne in 11 HO shells is 3.8×10^{10}. Thus, it is remarkable that even excitation energies calculated in model spaces selected down to a few symplectic irreps closely reproduce the experimental data.

3.3. Benchmark Studies and Nuclear Properties

This section summarizes the results of a series of benchmark studies showing that the SA-NCSM uses significantly smaller model space in comparison to the corresponding large complete $N_{\max}$ model space (or, equivalently, NCSM) without compromising the accuracy for various observables

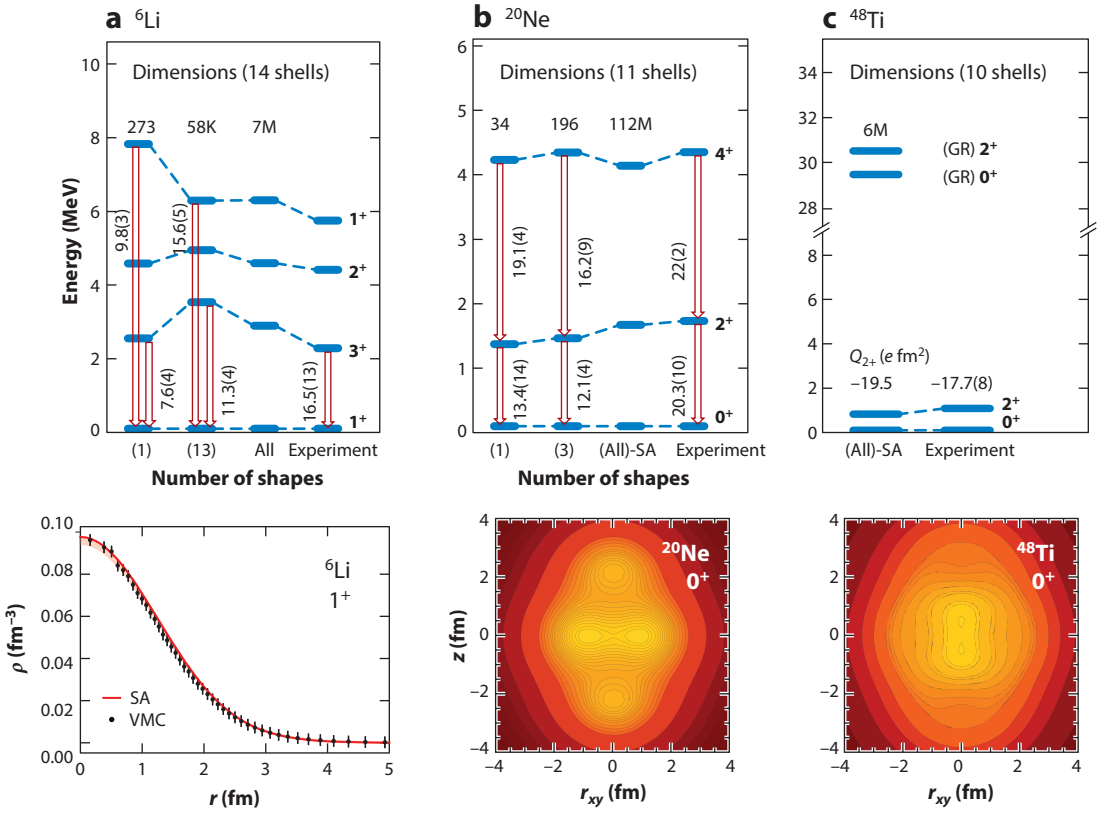

Figure 2

Energy spectra, $B(E2)$ transition strengths (in W.u.) or Q-quadrupole moments (in e fm^2), and one-body densities for (*a*) ^{6}Li, (*b*) ^{20}Ne, and (*c*) ^{48}Ti, based on ab initio SA-NCSM calculations with NNLO$_{\text{opt}}$. Energy spectra are labeled according to the dimensions of the largest model spaces used and the number of Sp(3, $\mathbb{R}$) irreps (*shapes*). Observables are reported for infinite model spaces, except calculations with all symplectic irreps (labeled "All") in complete or SA spaces that use $\hbar\Omega = 15$ MeV. Point-proton densities are shown for the largest model spaces (panel *a*, *red solid line*; panels *b* and *c*, *spatial profiles*), as well as for the single irrep (panel *a*, *red color band*). The ^{6}Li point-proton density is compared with VMC with AV18/Urbana IX (97). Abbreviations: GR, giant resonance; irrep, irreducible representation; SA, symmetry-adapted; SA-NCSM, symmetry-adapted no-core shell model; VMC, variational Monte Carlo. Energy spectra in panels *a* and *b* adapted with permission from Reference 1.

that probe nuclear properties. These include energies, point-particle rms radii, electric quadrupole and magnetic dipole moments, reduced $B(E2)$ transition strengths (19, 24), electron scattering form factors (25), and sum rules (26). Indeed, results for light nuclei (the illustrative examples of ^{4}He, ^{6}Li, and ^{12}C are presented below) agree with those of other ab initio approaches, such as the hyperspherical harmonics (HH) and the NCSM, as well as with variational Monte Carlo (VMC) and Green's function Monte Carlo (GFMC). After this discussion, we illustrate the capability of the SA concept to reach heavier nuclei, such as ^{32}Ne and ^{48}Ti (30).

For ^{4}He, Reference 26 compared SA-NCSM observables with exact solutions of the HH. We present selected results of this benchmark study, with a focus on the ground-state energy and point-proton rms radius of ^{4}He with the JISP16 and N3LO-EM potentials, as well as selected energy moments of the response function (i.e., sum rules). Response functions for electromagnetic probes are important because they are used to calculate cross sections and can

Table 1 Benchmark results for the SA framework compared with other ab initio methods for selected observables[a]

Nuclei	Observables	SA-NCSM	NCSM	Reference	Other methods	Reference	Experiment
^{4}He $0^+_{g.s.}$	BE (MeV)	28.2944(7)	28.2986(4)	26	28.300 (HH)	26	28.3
		26(1)*	25(1)*	26	25.3(1)* (HH)	26	
	Dipole NEWSR (e^2 fm^2)	0.94(2)*	0.95(3)*	26	0.945* (HH)	26	NA
	Monopole EWSR/NEWSR (MeV)	6.67(3)	6.63(1)	26	6.623(5) (HH)	26	NA
^{6}Li $1^+_{g.s.}$	BE (MeV)	30.45	30.95	19	27.0(1)** (VMC), 31.2(1)** (GFMC)	100	31.99
	r_p (fm)	2.11	2.13	19	2.46(2)** (VMC)	101	2.43[b]
		2.13***	2.14***				
	Q (e fm^2)	−0.080	−0.064	19	−0.33(18)** (VMC)	101	−0.0818(17)
	μ (μ_N)	+0.839	+0.838	19	+0.828(1)** (VMC)	101	+0.82205
^{12}C	BE (MeV)	85.95	87.90	24			92.16
	$E_{2^+_1}$ (MeV)	4.64	4.69	24			4.44
	$Q_{2^+_1}$ (e fm^2)	+3.735	+3.741	24			+6(3)
	$\mu_{1^+_1}$ (μ_N)	0.839	0.848	24			NA
	$B(M1; 1^+_1 \rightarrow 0^+_{g.s.})$ (μ_N^2)	0.012	0.013	24			0.0145(21)

[a]Values without uncertainties are given for N_{max} and $\hbar\Omega$ (the same N_{max} for both SA-NCSM and NCSM). Unless otherwise stated, calculations use the JISP16 potential, and unless otherwise stated, experimental data are from Reference 99.

[b]Deduced from the ^{6}Li charge radius of 2.56(5) fm (102).

Abbreviations: $B(M1)$, magnetic dipole transition strength; BE, binding energy; E, excitation energy; EWSR, energy-weighted sum rule; GFMC, Green's function Monte Carlo; g.s., ground state; HH, hyperspherical harmonics; NA, not available; NCSM, no-core shell model; NEWSR, non-energy-weighted sum rule; Q, electric quadrupole moment; r_p, point-proton root-mean-square radius; SA, symmetry-adapted; VMC, variational Monte Carlo; μ, magnetic dipole moment. Entries marked with an asterisk (*) indicate N3LO-EM *NN*; two asterisks (**), AV18/Urbana IX; three asterisks (***), NNLO$_{opt}$.

reveal information about the dynamical structure of the nucleus itself. While it is desirable to compute the full response function, it is sometimes easier to study its energy moments, which can be compared with experiment as well. The SA-NCSM calculations, when extrapolated to infinite spaces, are found to practically coincide with the HH and NCSM results (**Table 1**) while exhibiting very good convergence with the model-space size, parameterized by K_{max} for the HH and N_{max} for the SA-NCSM and NCSM (see **Figure 3*a***) for an illustrative example). Overall, sum rules, such as the non-energy-weighted sum rule (NEWSR), energy-weighted sum rule (EWSR), and inverse energy-weighted sum rule (IEWSR), for monopole, dipole, and quadrupole probes show agreement within 2σ between the HH results and the extrapolated SA-NCSM values for JISP16 (see **Table 1** for selected sum rules and interactions; for a complete set of values for JISP16, N3LO, and NNLO$_{opt}$, see tables II and III of 26). The extrapolated values for NCSM and SA-NCSM in **Table 1** are based on several model-space sizes up to 17 shells and a 10% variation in the $\hbar\Omega$ parameter; the HH results without uncertainties are reported at convergence. Note that all observables reported are translationally invariant, which is not trivial for sum rules calculated in many-body methods that use laboratory-frame coordinates and has been resolved (26) by a novel algorithm based on the Lawson procedure (98).

NEWSR: non-energy-weighted sum rule

EWSR: energy-weighted sum rule

IEWSR: inverse energy-weighted sum rule

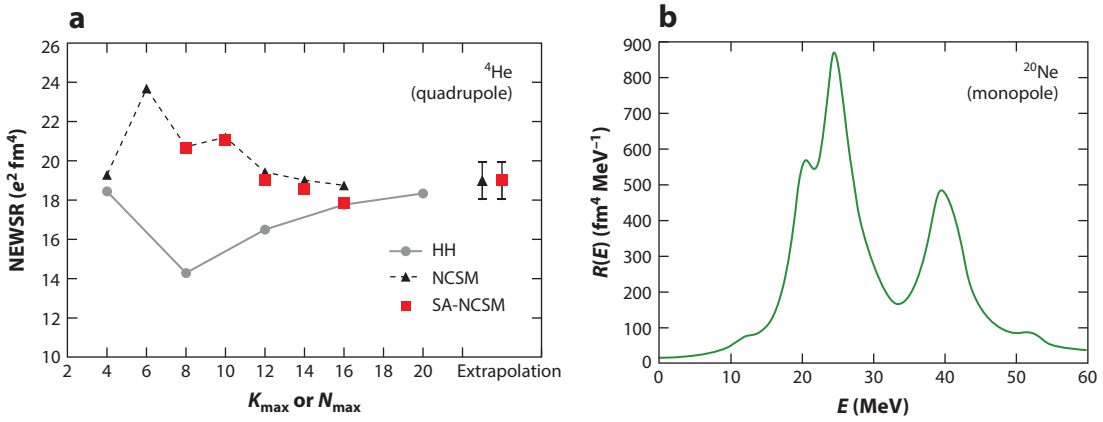

Figure 3

(*a*) Quadrupole NEWSR (translationally invariant) for ^{4}He as a function of the model-space size (K_{max} or N_{max}), based on ab initio HH and SA-NCSM ($\hbar\Omega = 25$ MeV) calculations with N3LO-EM interaction (*NN* only). (*b*) Lorentz integral transform (translationally invariant) for monopole transitions to the ^{20}Ne ground state versus excitation energy E for a Lorentzian kernel width of $\Gamma_{\mathfrak{L}} = 2$ MeV that yields the response function in the $\Gamma_{\mathfrak{L}} \to 0$ limit (26), based on ab initio SA-NCSM calculations with NNLO$_{opt}$ and $\hbar\Omega = 15$ MeV. Abbreviations: HH, hyperspherical harmonics; NCSM, no-core shell model; NEWSR, non-energy-weighted sum rule; SA-NCSM, symmetry-adapted no-core shell model. Panel *a* adapted with permission from Reference 26. Panel *b* adapted with permission from Reference 88.

Similarly, for the ^{6}Li ground state and low-lying isospin-zero states, Reference 19 has validated the use of selected SA spaces in comparison to the complete N_{max} model space, as illustrated in **Table 1** for selected observables for 14 shells, for $\hbar\Omega = 20$ MeV, and with JISP16 and NNLO$_{opt}$ *NN* interactions. Reference 25 compares these results with those of the ab initio VMC and GFMC methods that use the AV18 *NN* and Urbana IX 3*N* interactions (103, 104). Note the remarkable agreement between the results of the two methods, despite the use of realistic interactions that differ in construction and properties (e.g., nonlocal versus local). The close agreement between the SA-NCSM and VMC results holds also for the ^{6}Li point-proton density (**Figure 2*a***), where the SA-NCSM calculations span model spaces of 14 shells ($N_{max} = 12$) that include all symplectic irreps (for $\hbar\Omega = 20$ MeV) or only the single symplectic irrep, used to determine the extrapolated ^{6}Li energies and $B(E2)$ strengths shown in **Figure 2*a***.

Results for a heavier nucleus, ^{12}C, corroborate the findings for ^{4}He and ^{6}Li (24, 105). Selected SA-NCSM observables are listed in **Table 1** for 10 shells and $\hbar\Omega = 20$ MeV, and they practically coincide with the complete-space calculations. In addition, Reference 24 shows that the size of the model space and the number of nonzero Hamiltonian matrix elements—for SA selected spaces—grow slowly with the model-space size N_{max}.

Furthermore, the SA framework has been applied to observables that can be extracted from electron scattering and photoabsorption experiments. The longitudinal electric charge form factor has been studied (25) using ab initio SA-NCSM calculations for the 1^+ ground state of ^{6}Li, as shown in **Figure 4*a***, which compares SU(3) selected spaces in 14 shells with the corresponding complete model space. The agreement with both NCSM and experiment demonstrates that the symmetry considerations of the type we consider in the SA framework also properly treat excitations to higher HO shells relevant for typical momentum transfers, $q \lesssim 4$ fm^{-1} (25).

The electric dipole polarizability α_D can be extracted from photoabsorption experiments. Specifically, α_D can be deduced from the photoabsorption cross sections $\sigma_\gamma(E) = 4\pi^2 \alpha E R(E)$ by integrating the data (106, 107) with the proper energy weight, where $R(E)$ is the dipole response

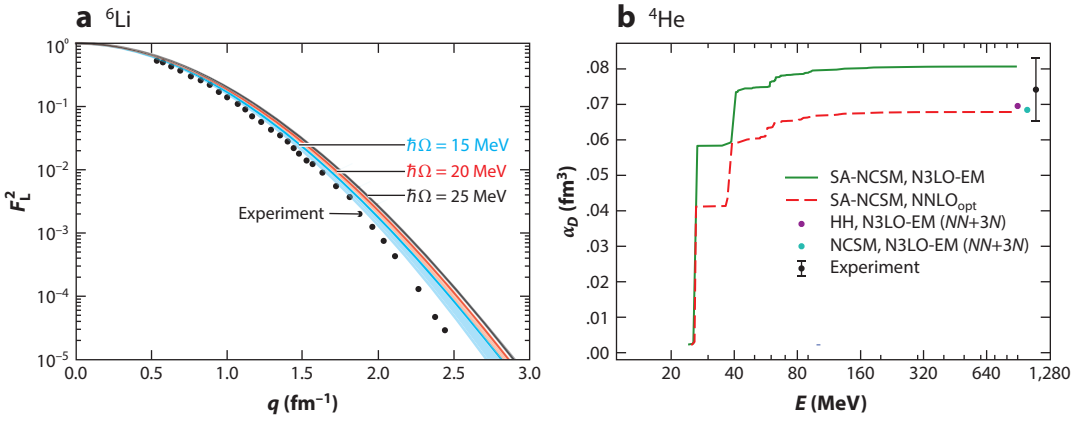

Figure 4

(*a*) Longitudinal electric charge form factor F_L^2 (translationally invariant and adjusted to account for the finite proton size) for the ^{6}Li ground state, based on ab initio SA-NCSM calculations with NNLO$_{opt}$ in various selected model spaces up through 14 shells (*light-colored bands*). Solid lines represent the corresponding complete model space. Electron scattering experimental data are from Reference 102. (*b*) Electric dipole polarizability α_D (translationally invariant) as a function of the excitation energy E, using ab initio HH calculations, along with SA-NCSM and NCSM calculations in a model space of 18 harmonic oscillator shells with an intershell distance of $\hbar\Omega = 25$ MeV. Abbreviations: HH, hyperspherical harmonics; NCSM, no-core shell model; SA-NCSM, symmetry-adapted no-core shell model. Panel *a* adapted with permission from Reference 25. Panel *b* adapted with permission from Reference 26.

function for a given excitation energy E and α is the fine-structure constant. The IEWSR for ^{4}He can be used to calculate α_D, using the relation $\alpha_D = 2\alpha \times$ IEWSR, which is compared with experiment (**Figure 4*b***). Specifically, Reference 26 has shown that the N3LO-EM yields a larger α_D value than the NNLO$_{opt}$, while both results fall within the experimental uncertainties. This result is consistent with earlier theoretical research that included the complementary 3*N* forces in the N3LO-EM and showed that they reduce the value of α_D by as much as 15% (108). Remarkably, the outcome for the N3LO-EM ($NN + 3N$), calculated in the HH (109) and the NCSM (110), closely agrees with that for the NNLO$_{opt}$ using only *NN* forces.

Within the SA framework, calculations up through medium-mass nuclei are feasible. For example, the first SA-NCSM calculations in 10 shells are available for ^{48}Ti (**Figure 2*c***), including its ground-state one-body density profile (in the body-fixed frame) and an estimate of the quadrupole moment of its lowest 2^+ state, which is in good agreement with experiment. These calculations use SA model spaces with approximately 6×10^6 basis states, in comparison to the infeasible number of 3×10^{13} for the corresponding complete model space.

As another illustrative example, we show structure observables for ^{20}Ne, together with its ground-state one-body density (**Figure 2*b***) and response to an isoscalar electric monopole probe, $M_0 = (1/2)\sum_i r_i^2$ (**Figure 3*b***). In **Figure 3*b***, the response is illustrated by the Lorentz integral transform (111, 112) for monopole transitions to the ^{20}Ne ground state using a Lorentzian kernel width of $\Gamma_{\mathfrak{L}} = 2$ MeV, which yields the response function in the $\Gamma_{\mathfrak{L}} \to 0$ limit. The first large peak is associated with a breathing mode, or giant monopole resonance (113), and can provide a stringent probe of incompressibility and nuclear saturation properties (114). Indeed, since the M_0 operator is a symplectic generator and does not mix symplectic irreps, the monopole response shown in **Figure 3*b*** tracks the contribution of the predominant shape of the ^{20}Ne ground state to all excited 0^+ states. It is not surprising, then, that the distribution and peak of the response are consistent with the results of Reference 1 (see the higher 0^+ states in **Figure 1*a***).

Indeed, Reference 1 suggests that the set of excited 0^+ states shown in **Figure 1*a***, with a non-negligible contribution of the 1p–1h excitations of the ground-state equilibrium shape, describes a fragmented giant monopole resonance with a centroid around 29 MeV and a typical wave function spread out to higher deformation due to vibrations (115), in contrast to the ground state. The different deformation content is clearly evident in the β–γ plots in **Figure 1*a***, which depict the deformation distribution within the same symplectic irrep for the ground state and the GR peak across the average deformation β and triaxiality γ.

4. NUCLEAR REACTIONS WITH SYMMETRY-ADAPTED BASIS

4.1. α-Induced Reactions

Partial widths are given by the decay rates of resonances into different open channels. They are not directly measurable, and extraction is model dependent to a greater or lesser extent. α widths and α-capture reactions of intermediate-mass nuclei are now feasible in the ab initio SA framework, including intermediate-mass nuclei along the path of XRB nucleosynthesis. In general, the formalism is applicable up through the medium-mass region with the ab initio SA-NCSM as well as for heavier nuclei, for instance, when nuclear fragments are described in the no-core symplectic shell model (NCSpM) with effective many-nucleon interaction (115–118). The NCSpM can reach ultralarge model spaces and has achieved successful microscopic descriptions of low-lying states in deformed $A = 8$–24 nuclei (117), particularly the elusive Hoyle state in ^{12}C and its first 2^+ and 4^+ excitations (116).

Modeling nuclear systems with cluster substructure represents a major challenge for many-particle approaches that build on realistic interactions. For light nuclei, there has been recent progress in ab initio descriptions of α-cluster systems including the GFMC method, with applications to the α-cluster structure of ^{8}Be and ^{12}C, along with electromagnetic transitions (103); the nuclear lattice EFT, with applications to the Hoyle state energy and the astrophysically relevant α–α scattering problem (35, 119, 120); and the HH method, with applications to GR modes in ^{4}He (121). Of particular note are recent developments that combine RGM with configuration-interaction methods (70, 122), as well as with ab initio NCSM and SA-NCSM (34, 42, 83; see Section 4.2.1). Reference 123 provides a review of cluster models, including some of the earliest techniques that treat particles within localized clusters, such as RGM (44, 124) and the related generator coordinate method (125), as well as molecular dynamics approaches (126, 127).

Reference 41 presents a new many-body technique for determining challenging α widths and asymptotic normalization coefficients (ANCs) utilizing ab initio SA-NCSM wave functions, with a focus on the ^{16}O(α,γ)^{20}Ne reaction rate. Indeed, the SA framework is ideal for addressing cluster substructures, as it enables the large model spaces needed for clustering and capitalizes on the complementary nature of the symplectic basis and the cluster basis (17, 128, 129). Several studies have taken advantage of this relationship by using a single SU(3) deformation for the clusters. Specifically, this approach has been used to describe the sub-Coulomb ^{12}C+^{12}C resonances of ^{24}Mg (130) that are of particular interest in astrophysics, as well as spectroscopic factors for α conjugate nuclei (that is, nuclei with multiples of two protons and two neutrons) (128, 129, 131). These studies have shown that some of the most important shell-model configurations can be expressed by exciting the relative-motion degree of freedom of the clusters. Furthermore, they have indicated that an approach that utilizes both the cluster and symplectic bases proves to be advantageous, especially since the model based on the cluster basis only, for clusters without excitations, tends to overestimate cluster decay widths and underestimate $E2$ transition rates (129).

Reference 41 reports the first α partial width of the lowest 1^- resonance, using ab initio ^{20}Ne wave functions. Specifically, for the partition into a- and A-particle clusters, the relative wave

function $ru_{cl}^{J^\pi}(r)$ is given by

$$u_{cl}^{J^\pi}(r) = \sum_\eta R_{\eta l}(r)\langle (A+a)\mathfrak{a} J^\pi M | (A\mathfrak{a}_1 I_1^{\pi_1}, a\mathfrak{a}_2 I_2^{\pi_2}) I, \eta l; J^\pi M\rangle, \qquad 2.$$

where the cluster system is defined for a channel $c = \{\mathfrak{a}, \mathfrak{a}_1, I_1^{\pi_1}, \mathfrak{a}_2, I_2^{\pi_2}, I\}$, which is labeled by the angular momentum (spin) and parity of each of the clusters and the total spin of the clusters I (the labels $\mathfrak{a}$, $\mathfrak{a}_1$, and $\mathfrak{a}_2$ denote all other quantum numbers needed to fully characterize their respective states) and a partial wave l. $R_{\eta l}(r)$ (where $\eta = 0, 1, 2, \ldots$ label $s, p, sd\ldots$ major HO shells) is the single-particle HO radial wave function. The integral of Equation 2 over r yields a spectroscopic factor. The overlap $\langle (A+a)\mathfrak{a} J^\pi M | (A\mathfrak{a}_1 I_1^{\pi_1}, a\mathfrak{a}_2 I_2^{\pi_2}) I, \eta l; J^\pi M\rangle$ is calculated for the $(A + a)$-body state of the composite system (in this example, ^{20}Ne) and the cluster configurations (in this example, $\alpha + ^{16}$O), using an efficacious Sp$(3, \mathbb{R})$ group-theoretical technique (41, 128, 129). In addition, using the microscopic R-matrix approach (132), $ru_{cl}^{J^\pi}(r)$ is matched at a channel radius with the exact solution to the Coulomb potential in the exterior (shown in **Figure 5** at long distances). In this way, one can obtain the two-cluster wave function that reflects the microscopic structure of the fragments while having the correct asymptotics, and hence calculate α widths for resonances and ANCs for bound states (41).

The new method is applied to the 1^- resonance in ^{20}Ne with a known natural width; because the state decays entirely through α emission, the natural width is the α partial width. Specifically, the $\alpha + ^{16}$O $l = 0$ and $l = 1$ wave functions are calculated using the ab initio SA-NCSM for the ^{20}Ne ground state and lowest 1^- state in 11 shells (**Figure 5**). Using extrapolations that do not depend on the channel radius, Reference 41 reports a value of $\Gamma_\alpha = 10(3)$ eV for the α partial width of the 1^- resonance, with uncertainty given by the variation in $\hbar\Omega$. Given that no parameters are fitted to nuclear data in this study, this estimate agrees reasonably well with the natural width of the ^{20}Ne 1^- state of 28(3) eV (133, 134). Note that while Reference 41 uses experimental thresholds, it emphasized the key role of correlations in developing cluster structures and collective modes, without which widths are drastically reduced.

This method also allows for first estimates for ANCs from ab initio descriptions of ^{20}Ne. The extrapolated ANC for the ground state is estimated to be $C_0 = 3.4 \pm 1.2 \times 10^3$ fm$^{-1/2}$ from ab initio SA-NCSM calculations. For the first excited 4^+ state in ^{20}Ne, which is in close proximity to the $\alpha + ^{16}$O threshold, the ANC is estimated from $N_{\max} = 14$ NCSpM calculations to be an order of magnitude larger (41).

The α widths can, in turn, be used to calculate α-capture reaction rates for narrow resonances of interest to astrophysics. This is achieved by use of the narrow resonance approximation, for which reaction rates are given by

$$N_A\langle \sigma v\rangle_r = \frac{1.539 \times 10^{11}}{(\mu_{A,a} T_9)^{3/2}} e^{-11.605 E_r/T_9} (\omega\gamma)_r. \qquad 3.$$

Here, T_9 is temperature in giga-Kelvin, $\mu_{A,a}$ is the reduced mass of the two clusters, E_r is the resonance energy in MeV, and the resonance strength is defined as

$$(\omega\gamma)_r = \frac{2J+1}{(2I_1+1)(2I_2+1)} \frac{\Gamma_\alpha \Gamma_\gamma}{\Gamma}. \qquad 4.$$

The use of the SA estimate for the α width Γ_α and Γ_γ/Γ extracted from the resonance strength of Reference 134 allows the contribution to the ^{16}O$(\alpha,\gamma)^{20}$Ne reaction rate through the 1.06-MeV 1^- resonance in ^{20}Ne to be calculated at astrophysically relevant temperatures. This calculated reaction rate is used as input to the Modules for Experiments in Stellar Astrophysics (MESA) code suite (135) to determine its impact on the abundance pattern produced during an XRB event (**Figure 5*b***). The MESA release (136) includes a model for an XRB with a constant accretion rate

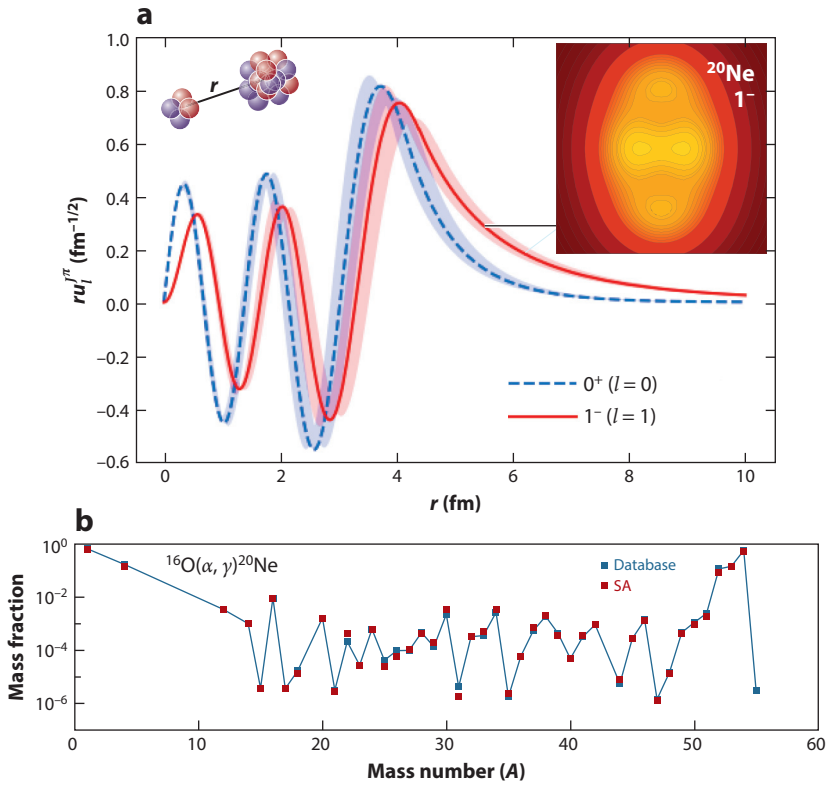

Figure 5

(*a*) α+^{16}O $l = 0$ and $l = 1$ relative wave functions from ab initio SA-NCSM calculations of the ^{20}Ne ground state and lowest 1^- state, respectively (with NNLO_{opt} and an intershell distance of $\hbar\Omega = 13$–17 MeV). (*b*) Difference between the initial mass fractions of the neutron star and the mass fractions 24 h after the burst begins based on the MESA X-ray burst simulation, showing good agreement between the pattern from the SA-calculated reaction rate and the pattern from the database reaction rate. All isotopes in the network with mass differences greater than 10^{-10} are shown. Abbreviations: MESA, Modules for Experiments in Stellar Astrophysics; SA, symmetry-adapted; SA-NCSM, symmetry-adapted no-core shell model. Figure adapted with permission from Reference 41, copyright American Physical Society.

and consistent burning across the entire surface of the neutron star, based on GS 1826-24, also known as the clocked burster (137). This model is designed for a nuclear network of 305 isotopes, including proton-rich isotopes up to ^{107}Te, but is also stable for a nuclear network of 153 isotopes up to ^{56}Fe, used in the present calculations. MESA includes all known reactions involving these nuclei, with reaction data taken from the REACLIB database (50). Remarkably, the SA-calculated reaction rate for the α-capture reaction $^{16}\text{O}(\alpha,\gamma)^{20}\text{Ne}$ yields practically the same XRB abundance pattern as the known reaction rate available in the REACLIB database (**Figure 5*b***).

4.2. Scattering and Reactions for a Single-Nucleon Projectile

The section presents a novel ab initio SA framework for reactions based on the RGM (42; 43; A. Mercenne et al., manuscript in preparation), applicable to nucleon scattering and capture reactions with light- to medium-mass nuclei at the astrophysically relevant energy regime (Section 4.2.1). As illustrative examples, we discuss results for neutron scattering off ^{16}O and ^{20}Ne (30). In addition, this section describes a state-of-the-art few-body approach to scattering at intermediate energies

based on the multiple scattering theory (46–48), with a focus on ab initio scattering cross sections and spin reaction observables at energies of ∼100–200 MeV (Section 4.2.2).

An important outcome of the RGM and multiple scattering approaches is an ab initio nucleon–nucleus effective potential. An alternative approach employed the Green's function framework, which was applied to low energies ($\lesssim$20 MeV per nucleon) using the self-consistent Green's function method (67) and the coupled-cluster method (68; see also 31). These studies built upon earlier theoretical frameworks, such as that introduced by Feshbach (138), leading to the Green's function formulation (139, 140), and that pioneered by Watson (141) and advanced by Kerman et al. (142) for elastic scattering of a nucleon from a nucleus, leading to the spectator expansion of the multiple scattering theory (143). Indeed, progress has recently been made in deriving microscopic optical potentials, which can then be used to provide cross sections for elastic scattering as well as input to (*d*, *p*) and (*d*, *n*) reactions (144). These studies have emphasized the need for realistic interactions that correctly reproduce rms radii as well as the importance of collective degrees of freedom to properly account for absorption.

4.2.1. Low energies: resonating group method. The RGM (44) is a microscopic method that uses fully antisymmetric wave functions, correctly treats the center-of-mass motion of the clusters, and takes internal correlations of the clusters into consideration. In the RGM, nucleons are organized within different groups, or clusters, "resonating" through the intercluster exchange of nucleons. The antisymmetrization between the different clusters enforces the Pauli exclusion principle. All of these features make this method particularly suitable for providing unified descriptions of nuclear structure and reaction observables. The SA-RGM builds upon the successful combination of the RGM and NCSM with *NN* and 3*N* interactions for light nuclei (45). With the use of the SA basis, the SA-RGM expands ab initio reaction theory to reactions of heavier nuclei and weakly bound systems near the drip lines for astrophysically relevant energies.

Traditionally, RGM has adopted generalized cluster wave functions as basis functions, which describe the motion of a system of two or more clusters. We consider two nuclear fragments, or two-cluster nuclear reactions. For two clusters *A* and *a*, the cluster states for a channel *c* are defined as (see Section 4.1)

$$\left|\Phi^{J^\pi}_{cr}\right\rangle = \left\{\left\{\left|A\mathfrak{a}_1 I_1^{\pi_1}\right\rangle \times \left|a\mathfrak{a}_2 I_2^{\pi_2}\right\rangle\right\}^I \times Y_\ell(\hat{r}_{A,a})\right\}^{J^\pi} \frac{\delta(r - r_{A,a})}{r r_{A,a}} \qquad 5.$$

for a relative distance between the clusters $r_{A,a}$ (see Equation 2). The $(A + a)$ nuclear wave function is given in terms of the cluster states,

$$\left|\Psi^{J^\pi}\right\rangle = \sum_c \int_r \mathrm{d}r r^2 \frac{g_c^{J^\pi}(r)}{r} \mathcal{A}_c \left|\Phi^{J^\pi}_{cr}\right\rangle, \qquad 6.$$

with unknown amplitudes $g_c^{J^\pi}(r)$ that are determined by solving the integral Hill–Wheeler equations (which follow from the Schrödinger equation):

$$\sum_c \int \mathrm{d}r r^2 \left[H_{c'c}(r', r) - E N_{c'c}(r', r)\right] \frac{g_c^{J^\pi}(r)}{r} = 0. \qquad 7.$$

Here, $H_{c'c}(r', r) = \langle \Phi^{J^\pi}_{c'r'} | \mathcal{A}_{c'} H \mathcal{A}_c | \Phi^{J^\pi}_{cr} \rangle$ is the Hamiltonian kernel and $N_{c'c}(r', r) = \langle \Phi^{J^\pi}_{c'r'} | \mathcal{A}_{c'} \mathcal{A}_c | \Phi^{J^\pi}_{cr} \rangle$ is the norm kernel, where $\mathcal{A}$ is the antisymmetrizer. The kernels are computed using the microscopic wave functions of the clusters that can be obtained in the ab initio NCSM and SA-NCSM. Once the kernels are computed, Equation 7 can be solved using the microscopic *R*-matrix approach (132).

In the SA-RGM, the target nucleus is described by SA-NCSM many-body wave functions. Specifically, a target state with spin and parity $I_1^{\pi_1}$ with projection M_1 is constructed in terms of

the SA basis:

$$\left|A\mathfrak{a}_1 I_1^{\pi_1} M_1\right\rangle = \sum_{\mathfrak{b}_1 \omega_1 \kappa_1 L_1 S_1} C_{\mathfrak{b}_1}^{\omega_1 \kappa_1 L_1 S_1} \left|\mathfrak{b}_1 \omega_1 \kappa_1 (L_1 S_1) I_1^{\pi_1} M_1\right\rangle, \qquad 8.$$

where the labels are defined, in general, as $\mathfrak{b} \equiv \{\ldots \omega_p \omega_n \rho N; S_p S_n\}$ and deformation $\omega \equiv (\lambda\, \mu)$. Protons and neutrons are labeled by p and n, respectively, and S labels the intrinsic spin (dots denote all additional quantum numbers). The SU(3) outer multiplicity ρ (91) results from the coupling of the proton deformation with that of neutrons to total deformation ω_1. As mentioned above, N labels the total HO excitations ($N \leq N_{\max}$). For a single-particle projectile, the SA-RGM basis states can be defined for a channel $\{\nu_1;\, \nu\} = \{\omega_1 \kappa_1 (L_1 S_1);\, \omega \kappa (LS)\}$ as

$$\left|\Phi_{\nu_1;\eta}^{\nu J^\pi M}\right\rangle = \sum_{\mathfrak{b}_1} C_{\mathfrak{b}_1}^{\nu_1} \left\{ |\mathfrak{b}_1 \omega_1 S_1\rangle \times \left|(\eta\, 0)\frac{1}{2}\right\rangle \right\}^{\nu J M}, \qquad 9.$$

where the SU(3) basis states for the target are coupled to the HO single-particle states $|(\eta\, 0)(1/2)\rangle$ of the projectile. Note that there is no dependence on the orbital momentum of the projectile, only on the shell number it occupies, η. Furthermore, the summation over $\mathfrak{b}_1$ implies that the SA-RGM basis requires only part of the information present in the SA basis.

The SA-RGM basis is used to calculate the RGM kernels, which is the main computational task in the RGM (45). One of the kernels is the norm kernel, which is the overlap between antisymmetrized nonorthogonal RGM basis states. It consists of a direct part (a Dirac delta function), which dominates at long relative distances, and an exchange part, which takes into account the Pauli principle at short distances. The exchange norm kernel is related to the permutation operator P, which exchanges the nucleon projectile with another nucleon within the target (45). The exchange norm kernel in the SA-RGM basis thus reduces to evaluating the following (and similarly for the Hamiltonian kernels):

$$\left\langle \Phi_{\nu_1';\eta'}^{\nu' J M} \middle| P \middle| \Phi_{\nu_1;\eta}^{\nu J M} \right\rangle = \delta_{\nu'\nu} \sum_{\omega_o S_o \rho_0} \Pi_{S_o S_1'} (-1)^{\eta+\eta'-\omega_o} (-1)^{S_1+\frac{1}{2}+S'} \begin{Bmatrix} S_1 & S_o & S_1' \\ \frac{1}{2} & S & \frac{1}{2} \end{Bmatrix}$$

$$\times \sqrt{\frac{\dim(\omega_o)}{\dim(\eta\, 0)}}\, U\left[\omega_1 \omega_o \omega'(\eta'\, 0);\, \omega_1' \rho_0 1(\eta\, 0) 11\right] \rho_{\eta\eta'}^{\rho_0 \omega_o S_o}(\nu_1';\, \nu_1). \qquad 10.$$

Here, $U[\ldots]$ is the SU(3) 6-$(\lambda\, \mu)$ recoupling coefficient (3), analogous to the SU(2) 6-j symbol, $\dim(\lambda\, \mu) = (1/2)(\lambda+1)(\mu+1)(\lambda+\mu+2)$. The SU(3) one-body density matrix elements are defined as

$$\rho_{\eta\eta'}^{\rho_0 \omega_o S_o}(\nu_1';\, \nu_1) = \sum_{\mathfrak{b}_1 \mathfrak{b}_1'} C_{\mathfrak{b}_1'}^{\nu_1'} C_{\mathfrak{b}_1}^{\nu_1} \left\langle \mathfrak{b}_1' \omega_1' S_1' \middle| \middle| \left\{ a_{(\eta\, 0)\frac{1}{2}}^\dagger \times \tilde{a}_{(0\, \eta')\frac{1}{2}} \right\}^{\omega_o S_o} \middle| \middle| \mathfrak{b}_1 \omega_1 S_1 \right\rangle_{\rho_0}. \qquad 11.$$

The matrix elements of the ρ density can be quickly computed in the SA basis through the use of an efficacious SU(3)-enabled vector–matrix–vector algorithm, and this can be done prior to the computation of the kernels. Notably, as a result of the Kronecker delta function in Equation 10, the exchange part of the norm kernel turns out to be block-diagonal in this basis. The reason is that the operator P is an SU(3) scalar and spin scalar, thereby preserving deformation and spin.

This procedure allows the kernels to be calculated, for each $J^\pi M$, through the SA-RGM channel basis of Equation 9, which depends only on the deformation, rotation, and spin of the target ν_1 (that is, $\omega_1 \kappa_1 L_1 S_1$) and on the deformation, rotation, and spin of the target-projectile system ν (that is, $\omega \kappa LS$). Thus, the SA offers two main advantages. First, the number of unique SU(3) configurations in the target wave function is manageable in comparison to the complete model-space

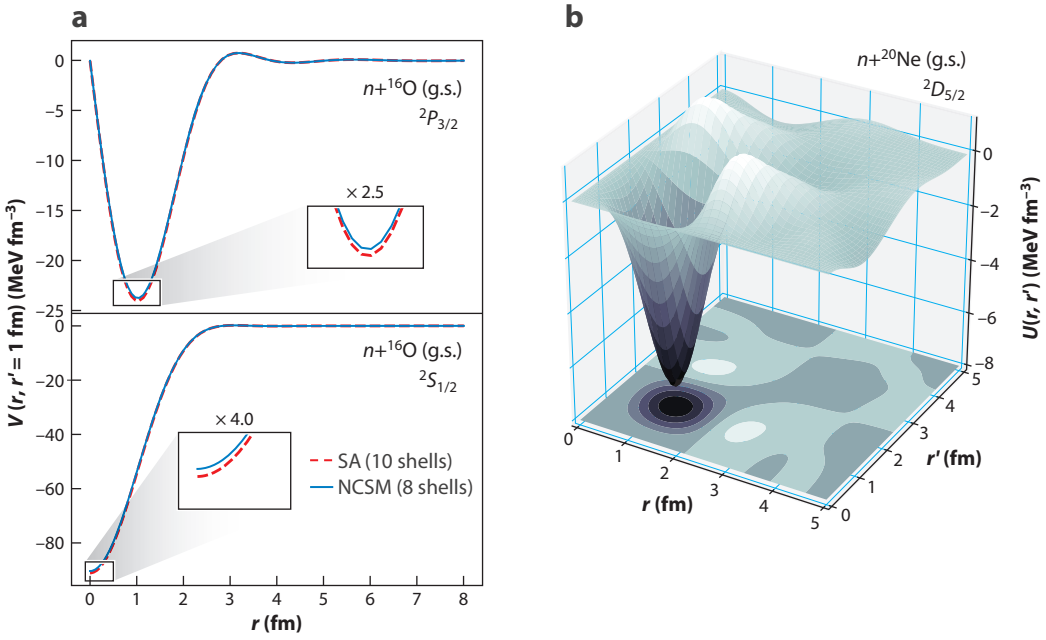

Figure 6

(*a*) Translationally invariant potential kernel (direct, *NN* only) for n+^{16}O(g.s.) in the ab initio SA-RGM approach using SA selected and complete model spaces (based on ab initio SA-NCSM calculations of ^{16}O with $\hbar\Omega = 16$ MeV and NNLO$_{\text{sat}}$ *NN*+3*N* in a model space of 10 shells; the projectile occupies 10 shells). (*b*) Effective neutron–nucleus potential for the ^{20}Ne ground state, where effects of the target excitations and antisymmetrization involving three nucleons are neglected (based on ab initio SA-NCSM calculations of ^{20}Ne with NNLO$_{\text{opt}}$ in a model space of 11 shells and an intershell distance of $\hbar\Omega = 15$ MeV). Abbreviations: g.s., ground state; SA-NCSM, symmetry-adapted no-core shell model; SA-RGM, symmetry-adapted resonating group method.

size. Second, a manageable number of configurations for the target-projectile system is based on SU(3) and SU(2) selection rules, namely $\omega = \omega_1 \times (\eta\, 0)$ and $S = S_1 \times (1/2)$. Thus, for example, for proton or neutron scattering off ^{20}Ne (with channels for the 0^+ ground state), there are only approximately 10^3–10^4 SA-RGM basis states for 7 to 13 shells, and only approximately 10^5 for ^{23}Mg when more target states are used (with channels for the $3/2^+$ ground state, $5/2^+$, and $7/2^+$). Interestingly, the number of unique deformed configurations for heavier targets such as neon and magnesium decrease in larger model spaces as dominant shapes are allowed to develop, thereby reducing shape mixing.

As discussed above, it is important to validate the use of the SA basis and selected model spaces to ensure that the selection does not remove configurations relevant for these reaction processes. Indeed, a benchmark study for ^{4}He and ^{16}O revealed that the selection has an almost negligible effect on the norm kernels and potential kernels $\langle \Phi^{J^\pi}_{c'r'} | \mathcal{A}_{c'} V \mathcal{A}_c | \Phi^{J^\pi}_{cr} \rangle$ (42; A. Mercenne et al., manuscript in preparation), which are used as input to calculate phase shifts and cross sections. An example is illustrated here for the direct potential kernel of n+^{16}O($0^+_{\text{g.s.}}$) (similarly for a proton projectile), with NNLO$_{\text{sat}}$ up to 10 shells for two partial waves $S_{1/2}$ and $P_{3/2}$ (**Figure 6*a***). Note that in these calculations the 3*N* forces are included as a mass-dependent monopole interaction (145), which has an effect on binding energies. For example, for the ^{16}O ground-state energy, the seven-shell 3*N* contribution is 20.46 MeV, resulting in a total energy of −127.97 MeV for $N_{\max} = 8$ and $\hbar\Omega = 16$ MeV, which agrees with the experimental value of −127.62 MeV.

In the SA-RGM framework, one starts from an ab initio description of all particles involved and derives the Hamiltonian kernel, which, when orthogonalized, yields nonlocal effective nucleon–nucleus interactions for the channels under consideration. For a single channel, if the effects of the target excitations are neglected, the nonlocal effective nucleon–nucleus interaction can be calculated for each partial wave, as illustrated in **Figure 6*b*** for $n+^{20}\mathrm{Ne}(0^+_{\mathrm{g.s.}})$ with $\mathrm{NNLO}_{\mathrm{opt}}$ in 11 shells. While these calculations limit the antisymmetrization to only two nucleons, this is a first step toward constructing effective nucleon–nucleus potentials for light- and medium-mass nuclei for astrophysically relevant energies.

4.2.2. Intermediate energies: multiple scattering method. The ab initio fully consistent framework of the spectator expansion of the multiple scattering theory was developed at leading order (48) to describe elastic scattering at intermediate energies. It capitalizes on the concept that the two-body interaction between the projectile and the nucleons inside the target nucleus plays a dominant role. Thus, the leading-order term involves the interaction of the projectile and one of the target nucleons, the second-order term involves the projectile interacting with two target nucleons, and so forth. With the goal of deriving an effective nucleon–nucleus potential, the effective potential operator is expanded in terms of active particles (146). At leading order (two active particles), a consistent treatment requires the use of an *NN* interaction to calculate the *NN* transition amplitude (describing the interaction between the projectile and the struck target nucleon), as well as the microscopic structure of the target nucleus that enters by means of one-body nuclear densities (for details, see 48). Note that the 3*N* effects enter only at the next order of the spectator expansion and require two-body nuclear densities along with a solution to a three-body problem for three active nucleons.

A series of studies constructed the leading-order ab initio effective nucleon–nucleus potential, which is nonlocal and energy dependent (48, 49, 148). This potential has been used to calculate reaction observables, such as cross sections and analyzing power A_y, in helium isotopes and other light nuclei, including ^{12}C and ^{16}O. For the first time, the nuclear densities of the target in the multiple scattering theory have been derived from ab initio calculations. The outcome of these studies is that the differential cross section and A_y as a function of the center-of-mass angle, or equivalently the momentum transfer q, exhibits remarkable agreement with experimental data when the chiral $\mathrm{NNLO}_{\mathrm{opt}}$ *NN* potential is employed (see **Figure 7*a*** for ^{4}He).

Similarly to reaction observables at low energies (Section 4.2.1), we show that the SA selected and complete model spaces practically coincide for the angular distribution of the differential cross section and the analyzing power for protons on a ^{4}He target at a laboratory projectile kinetic energy of 200 MeV, using the N3LO-EM chiral potential (**Figure 7*a***). Furthermore, the SA framework can extend calculations to intermediate-mass nuclei; specifically, the ab initio $^{20}\mathrm{Ne}(p, p)^{20}\mathrm{Ne}$ differential cross section at 100 MeV and 200 MeV exhibits a slight decrease in comparison to smaller model spaces where the predominant shape is not fully developed (**Figure 7*b***). Indeed, missing collective correlations have been suggested to reduce absorption in scattering at lower energies (68). The results in **Figure 7*b*** pave the way toward exploring proton and neutron scattering on intermediate- and medium-mass targets, including the role of collectivity and clustering.

5. SUMMARY AND OUTLOOK

In this review, we have discussed recent ab initio developments made possible by the use of the SA basis, which can reach ultralarge shell-model spaces in light- through medium-mass nuclei. First, the use of the SA basis is essential for structure observables, especially for precise descriptions of

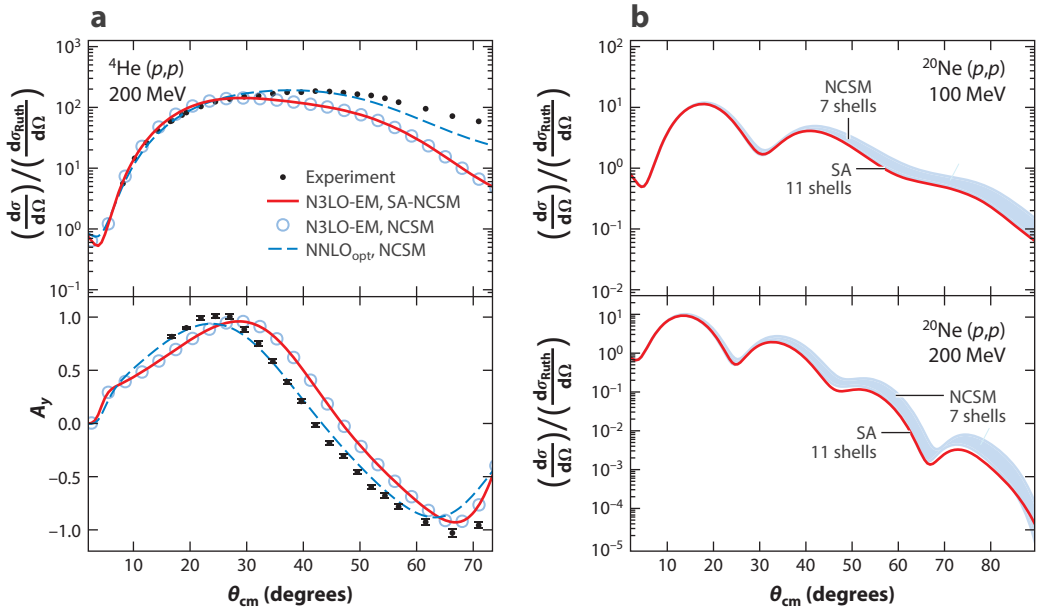

Figure 7

(*a*) Angular distribution of the differential cross section divided by the Rutherford cross section and analyzing power for elastic proton scattering on ^{4}He at a laboratory kinetic energy of 200 MeV as a function of θ_{cm}, showing perfect agreement between SA selected and complete (NCSM) model spaces of 15 shells ($N_{max} = 14$) with the N3LO-EM NN interaction and $\hbar\Omega = 25$ MeV. Also shown are calculations with the NNLO$_{opt}$ NN chiral potential, in good agreement with experiment. Experimental data are from Reference 147. (*b*) Angular distribution of the differential cross section divided by the Rutherford cross section for (*top*) 100-MeV and (*bottom*) 200-MeV proton laboratory kinetic energy on a ^{20}Ne target (the calculations use NNLO$_{opt}$ with an intershell distance of $\hbar\Omega = 15$ MeV for SA and $\hbar\Omega = 14$–16 MeV for the NCSM band). Abbreviations: NCSM, no-core shell model; SA, symmetry-adapted; θ_{cm}, center-of-mass angle. Panel *a* adapted with permission from Reference 48, copyright American Physical Society.

cluster formations in nuclei (e.g., in ^{20}Ne) or of collectivity in medium-mass nuclei, such as ^{48}Ti, which is of interest for neutrinoless double-β-decay experiments that aim to determine whether the neutrino is its own antiparticle (149, 150). Second, the SA basis enables couplings to the continuum, through excitations that are otherwise inaccessible and with the help of the SA-RGM basis, which accounts for decays to open channels. These features are critical for calculating reaction observables and for deriving nucleon–nucleus potentials rooted in first principles, as discussed in this review in the context of both the SA-RGM approach for the astrophysically relevant energy regime and the multiple scattering method at intermediate energies. In many cases, results are highly sensitive to the microscopic structure; for instance, nucleon scattering and capture reactions at low energies are driven by a few open channels and isolated resonances, whereas collectivity and clustering are essential for α-capture reactions and for deformed target or beam isotopes. As these approaches build upon first principles, they can probe features of the NN interaction that are relevant to reactions but remain unconstrained in fits to phase shifts or few-nucleon observables.

In short, with the help of high-performance computing resources, the use of the SA concept in ab initio studies represents a powerful tool for the study of the structure and reactions of nuclei, and it is manageable as well as expandable. In other words, one expects to be able to extend the reach of the SA scheme from applications that are feasible today to the larger spaces and heavier nuclear systems of tomorrow, utilizing at each stage the predictive power of the ab initio approach to inform and support current and planned experiments.

SUMMARY POINTS

1. The SA basis exploits dominant symmetry in atomic nuclei [such as the symplectic Sp(3, $\mathbb{R}$) symmetry, which does not mix nuclear shapes] and provides microscopic descriptions of nuclei in terms of collective shapes (equilibrium shapes with their vibrations) that rotate.
2. Only a few shapes (a few symplectic irreps) dominate in low-lying nuclear states, thereby making significantly reduced SA selected model spaces ideal for study and prediction of various observables for spherical and deformed open-shell nuclei.
3. Small model spaces are sufficient to develop many shapes relevant to low-lying states, but they often omit the vibrations of largely deformed equilibrium shapes and spatially extended modes such as clustering. This problem is what is remedied by the use of selected model spaces.
4. SA model spaces include all possible shapes (equivalently, all particle–hole configurations) up to a given total particle-excitation energy and are selected only for larger energies, implying that single-particle and collective degrees of freedom enter on an equal footing.
5. In the SA basis, the center-of-mass motion can be factored out exactly.
6. Ab initio SA-NCSM calculations are now feasible for structure, reaction, and scattering observables of nuclei ranging from light to medium mass.

DISCLOSURE STATEMENT

The authors are not aware of any affiliations, memberships, funding, or financial holdings that might be perceived as affecting the objectivity of this review.

ACKNOWLEDGMENTS

We acknowledge invaluable discussions with J.P. Draayer, S. Bacca, C. Elster, J.E. Escher, and S. Quaglioni, as well as D.J. Rowe, J.L. Wood, G. Rosensteel, J.P. Vary, P. Maris, C.W. Johnson, and D. Langr. We also thank R.B. Baker, G.H. Sargsyan, A.C. Dreyfuss, and M. Burrows for providing important results. The writing of this review was supported in part by the US National Science Foundation (OIA-1738287, PHY-1913728), the Southeastern Universities Research Association, the Czech Science Foundation (16-16772S), and the US Department of Energy (DE-SC0019521). It benefited from high-performance computational resources provided by Louisiana State University (**https://www.hpc.lsu.edu/**); the National Energy Research Scientific Computing Center, a US Department of Energy Office of Science User Facility operated under contract DE-AC02-05CH11231; and the Frontera computing project at the Texas Advanced Computing Center, made possible by National Science Foundation award OAC-1818253.

LITERATURE CITED

1. Dytrych T, et al. *Phys. Rev. Lett.* 124:042501 (2020)
2. Rowe DJ. *Rep. Prog. Phys.* 48:1419 (1985)
3. Draayer JP, Akiyama Y. *J. Math. Phys.* 14:1904 (1973)
4. Draayer J, Weeks K, Rosensteel G. *Nucl. Phys. A* 413:215 (1984)

5. Blokhin A, Bahri C, Draayer J. *Phys. Rev. Lett.* 74:4149 (1995)
6. Launey KD, Dytrych T, Draayer JP. *Prog. Part. Nucl. Phys.* 89:101 (2016)
7. Rosensteel G, Rowe DJ. *Phys. Rev. Lett.* 38:10 (1977)
8. Rosensteel G, Rowe DJ. *Ann. Phys. N. Y.* 126:343 (1980)
9. Rowe DJ. *Prog. Part. Nucl. Phys.* 37:265 (1996)
10. Heyde K, Wood JL. *Rev. Mod. Phys.* 83:1467 (2011)
11. Wood JL. In *Emergent Phenomena in Atomic Nuclei from Large-Scale Modeling: A Symmetry-Guided Perspective*, ed. KD Launey, p. 1. Singapore: World Sci. (2017)
12. Rowe DJ, Wood JL. *J. Phys. G* 45:06LT01 (2018)
13. Elliott JP. *Proc. R. Soc. A* 245:128 (1958)
14. Elliott JP. *Proc. R. Soc. A* 245:562 (1958)
15. Elliott JP, Harvey M. *Proc. R. Soc. A* 272:557 (1963)
16. Hecht KT, Adler A. *Nucl. Phys. A* 137:129 (1969)
17. Hecht KT, Zahn W. *Nucl. Phys. A* 318:1 (1979)
18. Dytrych T, et al. *Phys. Rev. Lett.* 98:162503 (2007)
19. Dytrych T, et al. *Phys. Rev. Lett.* 111:252501 (2013)
20. Bedaque PF, van Kolck U. *Annu. Rev. Nucl. Part. Sci.* 52:339 (2002)
21. Epelbaum E, et al. *Phys. Rev. C* 66:064001 (2002)
22. Entem DR, Machleidt R. *Phys. Rev. C* 68:041001 (2003)
23. Rowe D. *AIP Conf. Proc.* 1541:104 (2013)
24. Dytrych T, et al. *Comput. Phys. Commun.* 207:202 (2016)
25. Dytrych T, et al. *Phys. Rev. C* 91:024326 (2015)
26. Baker RB, et al. *Phys. Rev. C* 102:014320 (2020)
27. Ruotsalainen P, et al. *Phys. Rev. C* 99:051301 (2019)
28. Henderson J, et al. *Phys. Lett. B* 782:468 (2018)
29. Williams J, et al. *Phys. Rev. C* 100:014322 (2019)
30. Launey KD, et al. *AIP Conf. Proc.* 2038:020004 (2018)
31. Johnson CW, et al. *J. Phys. G* 47:123001 (2020)
32. Nollett K, et al. *Phys. Rev. Lett.* 99:022502 (2007)
33. Hagen G, Dean D, Hjorth-Jensen M, Papenbrock T. *Phys. Lett. B* 656:169 (2007)
34. Quaglioni S, Navrátil P. *Phys. Rev. Lett.* 101:092501 (2008)
35. Elhatisari S, et al. *Nature* 528:111 (2015)
36. Zhang X, et al. *Phys. Rev. Lett.* 125:112503 (2020)
37. Bacca S, et al. *Phys. Rev. C* 90:064619 (2014)
38. Navrátil P, Quaglioni S. *Phys. Rev. Lett.* 108:042503 (2012)
39. Girlanda L, et al. *Phys. Rev. Lett.* 105:232502 (2010)
40. Hupin G, Quaglioni S, Navrátil P. *Nat. Commun.* 10:351 (2019)
41. Dreyfuss AC, et al. *Phys. Rev. C* 102:044608 (2020)
42. Mercenne A, et al. In *Recent Progress in Few-Body Physics: Proceedings of the 22nd International Conference on Few-Body Problems in Physics*, ed. N Orr, M Płoszajczak, F Marqués, J Carbonell, p. 253. Berlin: Springer. Springer Proc. Phys. 238 (2020)
43. Mercenne A, et al. In *Proceedings of the 6th International Workshop on Compound-Nuclear Reactions and Related Topics* (*CNR*18*), ed. J Escher, et al., p. 73. Berlin: Springer (2021)
44. Wildermuth K, Tang Y. *A Unified Theory of the Nucleus*. Braunschweig, Ger.: Vieweg (1977)
45. Quaglioni S, Navrátil P. *Phys. Rev. C* 79:044606 (2009)
46. Elster C, Weppner S, Chinn C. *Phys. Rev. C* 56:2080 (1997)
47. Dussan H, et al. *Phys. Rev. C* 90:061603 (2014)
48. Burrows M, et al. *Phys. Rev. C* 102:034606 (2020)
49. Burrows M, et al. *Phys. Rev. C* 97:024325 (2018)
50. Cyburt RH, et al. *Astrophys. J. Suppl.* 189:240 (2010)

51. Wolf C, et al. *Phys. Rev. Lett.* 122:232701 (2019)
52. Galloway DK, et al. *Astrophys. J. Suppl.* 179:360 (2008)
53. Brune CR, Davids B. *Annu. Rev. Nucl. Part. Sci.* 65:87 (2015)
54. Wiescher M, Käppeler F, Langanke K. *Annu. Rev. Astron. Astrophys.* 50:165 (2012)
55. deBoer RJ, et al. *Rev. Mod. Phys.* 89:035007 (2017)
56. Farmer R, et al. *Astrophys. J. Lett.* 902:L36 (2020)
57. Croon D, McDermott SD, Sakstein J. arXiv:2007.07889 [gr-qc] (2020)
58. Abbott BP, et al. *Phys. Rev. Lett.* 119:161101 (2017)
59. Surman R, Beun J, McLaughlin GC, Hix WR. *Phys. Rev. C* 79:045809 (2009)
60. Escher JE, et al. *Rev. Mod. Phys.* 84:353 (2012)
61. Escher JE, et al. *Phys. Rev. Lett.* 121:052501 (2018)
62. Mahzoon MH, Atkinson MC, Charity RJ, Dickhoff WH. *Phys. Rev. Lett.* 119:222503 (2017)
63. Fattoyev FJ, Piekarewicz J, Horowitz CJ. *Phys. Rev. Lett.* 120:172702 (2018)
64. Furumoto T, Tsubakihara K, Ebata S, Horiuchi W. *Phys. Rev. C* 99:034605 (2019)
65. Weppner S, Penney R, Diffendale G, Vittorini G. *Phys. Rev. C* 80:034608 (2009)
66. Koning A, Delaroche J. *Nucl. Phys. A* 713:231 (2003)
67. Idini A, Barbieri C, Navrátil P. *Phys. Rev. Lett.* 123:092501 (2019)
68. Rotureau J, et al. *Phys. Rev. C* 95:024315 (2017)
69. Michel N, Nazarewicz W, Płoszajczak M, Bennaceur K. *Phys. Rev. Lett.* 89:042502 (2002)
70. Mercenne A, Michel N, Płoszajczak M. *Phys. Rev. C* 99:044606 (2019)
71. Arcones A, et al. *Prog. Part. Nucl. Phys.* 94:1 (2017)
72. Carlson J, et al. *Prog. Part. Nucl. Phys.* 94:68 (2017)
73. Fonseca AC, Deltuva A. *Few-Body Syst.* 58:46 (2017)
74. Deltuva A, Fonseca AC. *Phys. Rev. C* 95:024003 (2017)
75. Lazauskas R. *Phys. Rev. C* 97:044002 (2018)
76. Viviani M, et al. *Phys. Rev. C* 95:034003 (2017)
77. Lovell A, Nunes F. *J. Phys. G* 42:034014 (2015)
78. Hergert H. *Front. Phys.* 8:379 (2020)
79. Rotureau J, et al. *Phys. Rev. Lett.* 97:110603 (2006)
80. Fossez K, Rotureau J, Michel N, Płoszajczak M. *Phys. Rev. Lett.* 119:032501 (2017)
81. De Grancey F, et al. *Phys. Lett. B* 758:26 (2016)
82. Navrátil P, Vary JP, Barrett BR. *Phys. Rev. Lett.* 84:5728 (2000)
83. Barrett B, Navrátil P, Vary J. *Prog. Part. Nucl. Phys.* 69:131 (2013)
84. Shirokov A, Vary J, Mazur A, Weber T. *Phys. Lett. B* 644:33 (2007)
85. Wiringa RB, Stoks VGJ, Schiavilla R. *Phys. Rev. C* 51:38 (1995)
86. Ekström A, et al. *Phys. Rev. Lett.* 110:192502 (2013)
87. Ekström A, et al. *Phys. Rev. C* 91:051301 (2015)
88. Launey KD, et al. *Eur. Phys. J. Spec. Top.* 229:2429 (2020)
89. Verhaar BJ. *Nucl. Phys.* 21:508 (1960)
90. Hecht KT. *Nucl. Phys. A* 170:34 (1971)
91. Draayer JP, Leschber Y, Park SC, Lopez R. *Comput. Phys. Commun.* 56:279 (1989)
92. Langr D, Dytrych T, Launey KD, Draayer JP. *Int. J. High Perform. Comput. Appl.* 33:522 (2019)
93. Oberhuber T, et al. *Discret. Contin. Dyn. Syst. S* S14(3):1111 (2021)
94. Johnson CW. *Phys. Rev. C* 91:034313 (2015)
95. Johnson CW. *Phys. Rev. Lett.* 124:172502 (2020)
96. McCoy AE, Caprio MA, Dytrych T, Fasano PJ. *Phys. Rev. Lett.* 125:102505 (2020)
97. Brida I, Pieper SC, Wiringa RB. *Phys. Rev. C* 84:024319 (2011)
98. Gloeckner DH, Lawson RD. *Phys. Lett. B* 53:313 (1974)
99. Tilley DR, et al. *Nucl. Phys. A* 708:3 (2002)
100. Wiringa RB, Schiavilla R. *Phys. Rev. Lett.* 81:4317 (1998)
101. Pudliner BS, et al. *Phys. Rev. C* 56:1720 (1997)

102. Li GC, Sick I, Whitney RR, Yearian MR. *Nucl. Phys. A* 162:583 (1971)
103. Carlson J, et al. *Rev. Mod. Phys.* 87:1067 (2015)
104. Lynn J, Tews I, Gandolfi S, Lovato A. *Annu. Rev. Nucl. Part. Sci.* 69:279 (2019)
105. Sargsyan GH, et al. *Phys. Rev. C* 103:044305 (2021)
106. Arkatov YM, et al. *Sov. J. Nucl. Phys.* 19:598 (1974)
107. Arkatov YM, et al. *Sov. J. Nucl. Phys.* 31:726 (1980)
108. Gazit D, et al. *Phys. Rev. C* 74:061001 (2006)
109. Ji C, Nevo Dinur N, Bacca S, Barnea N. *Phys. Rev. Lett.* 111:143402 (2013)
110. Stetcu I, et al. *Phys. Rev. C* 79:064001 (2009)
111. Efros VD, Leidemann W, Orlandini G. *Phys. Lett. B* 338:130 (1994)
112. Bacca S, et al. *Phys. Rev. Lett.* 111:122502 (2013)
113. Baker R. *Electromagnetic sum rules and response functions from the symmetry-adapted no-core shell model*. PhD Thesis, Louisiana State Univ., Baton Rouge (2019)
114. Garg U, Colò G. *Prog. Part. Nucl. Phys.* 101:55 (2018)
115. Bahri C, Rowe DJ. *Nucl. Phys. A* 662:125 (2000)
116. Dreyfuss AC, et al. *Phys. Lett. B* 727:511 (2013)
117. Tobin GK, et al. *Phys. Rev. C* 89:034312 (2014)
118. Dreyfuss AC, et al. *Phys. Rev. C* 95:044312 (2017)
119. Epelbaum E, Krebs H, Lee D, Meissner U-G. *Phys. Rev. Lett.* 106:192501 (2011)
120. Rupak G, Lee D. *Phys. Rev. Lett.* 111:032502 (2013)
121. Bacca S, Barnea N, Leidemann W, Orlandini G. *Phys. Rev. Lett.* 110:042503 (2013)
122. Kravvaris K, Volya A. *Phys. Rev. C* 100:034321 (2019)
123. Freer M, et al. *Rev. Mod. Phys.* 90:035004 (2018)
124. Wheeler JA. *Phys. Rev.* 52:1107 (1937)
125. Horiuchi H. *Prog. Theor. Phys.* 43:375 (1970)
126. Kanada-En'yo Y. *Phys. Rev. Lett.* 81:5291 (1998)
127. Chernykh M, et al. *Phys. Rev. Lett.* 98:032501 (2007)
128. Suzuki Y. *Nucl. Phys. A* 448:395 (1986)
129. Suzuki Y, Hecht KT. *Nucl. Phys. A* 455:315 (1986)
130. Suzuki Y, Hecht KT. *Nucl. Phys. A* 388:102 (1982)
131. Hecht KT, Reske EJ, Seligman TH, Zahn W. *Nucl. Phys. A* 356:146 (1981)
132. Descouvemont P, Baye D. *Rep. Prog. Phys.* 73:3 (2010)
133. MacArthur JD, Evans HC, Leslie JR, Mak HB. *Phys. Rev. C* 22:356 (1980)
134. Constantini H, et al. *Phys. Rev. C* 82:035802 (2010)
135. Paxton B, et al. *Astrophys. J. Suppl.* 243:10 (2019)
136. Paxton B, et al. *Astrophys. J. Suppl.* 220:15 (2015)
137. Ubertini P, et al. *Astrophys. J. Lett.* 514:L27 (1999)
138. Feshbach H. *Ann. Phys. N. Y.* 5:357 (1958)
139. Capuzzi F, Mahaux C. *Ann. Phys. N. Y.* 281:223 (2000)
140. Escher J, Jennings BK. *Phys. Rev. C* 66:034313 (2002)
141. Watson KM. *Phys. Rev.* 89:575 (1953)
142. Kerman AK, McManus H, Thaler RM. *Ann. Phys.* 8:551 (1959)
143. Siciliano ER, Thaler RM. *Phys. Rev. C* 16:1322 (1977)
144. Rotureau J, Potel G, Li W, Nunes FM. *J. Phys. G* 47:065103 (2020)
145. Launey KD, Dytrych T, Draayer JP. *Phys. Rev. C* 84:044003 (2012)
146. Chinn CR, Elster C, Thaler RM. *Phys. Rev. C* 47:2242 (1993)
147. Moss GA, et al. *Phys. Rev. C* 21:1932 (1980)
148. Burrows M, et al. *Phys. Rev. C* 99:044603 (2019)
149. Yao JM, et al. *Phys. Rev. Lett.* 124:232501 (2020)
150. Novario SJ, et al. arXiv:2008.09696 [nucl-th] (2020)

RELATED RESOURCES

1. Kota VKB. SU(3) *Symmetry in Atomic Nuclei*. Singapore: Springer (2020)
2. Launey KD, ed. *Emergent Phenomena in Atomic Nuclei from Large-Scale Modeling: A Symmetry-Guided Perspective*. Singapore: World Sci. (2017)
3. Rowe DJ, Wood JL. *Fundamentals of Nuclear Models: Foundational Models*. Singapore: World Sci. (2010)
4. Thompson IJ, Nunes FM. *Nuclear Reactions for Astrophysics*. Cambridge, UK: Cambridge Univ. Press (2009)
5. Suzuki Y, Lovas RG, Yabana K, Varga K. *Structure and Reactions of Exotic Nuclei*. London/New York: Taylor & Francis (2003)

Annual Review of Nuclear and Particle Science

Volume 71, 2021

Contents

Errata

An online log of corrections to *Annual Review of Nuclear and Particle Science* articles may be found at http://www.annualreviews.org/errata/nucl